Appraisal of Resistivity Inversion Models with Convolutional Variational Encoder-Decoder Network

Bibin Wilson*, Anand Singh*, Amit Sethi†

***Abstract*—Recovering the actual subsurface electrical resistivity properties from the electrical resistivity tomography data is challenging because the inverse problem is nonlinear and ill-posed. This paper proposes a Variaional Encoder-Decoder (VED) based network to obtain resistivity model, which maps the apparent resistivity data(input) to true resistivity data(output). Since deep learning models are highly dependent on training sets and providing a meaningful geological resistivity model is complex, we have first trained our deep learning method to construct many realistic resistivity synthetic models. Our algorithm automatically constructs an apparent resistivity pseudo-section from these resistivity models. We further computed the resistivity from two different neural architectures for comparison – UNet, and attention UNet with and without input depth encoding apparent data. In the end, we have compared our deep learning results with traditional inversion and borewell data on apparent resistivity datasets collected for aquifer mapping in the hard rock terrain of the West Medinipur district of West Bengal, India. A detailed qualitative and quantitative evaluation reveals that our VED approach is the most effective for the inversion compared to other networks considered.**

***Index Terms*—Electrical Resistivity Tomography, Deep Learning, Inverse Problem, Conductivity Distribution.**

I. Introduction

With a wide range of geophysical and environmental applications, Electrical Resistivity Tomography (ERT) is a low-cost geophysical approach [1].The field measurement procedure is straightforward in an ERT investigation. A known electrical current is sent using two metal electrodes and the potential differences through another pair of metal electrodes is measured. The electrodes can be located on the surface or in boreholes. The measured electrical currents and potential in the apparent resistivity of the subsurface are transformed based on the used electrode array configurations. Inverse modeling provides a mathematical framework to obtain an actual subsurface resistivity distribution from the measured field apparent resistivity datasets. Since the number of measured ERT data points is less than the number of resistivity model points, the inverse problem is intrinsically non-unique and ill-posed [2]. It means that there are too many resistivity models whose response can fit the measured resistivity data sets within a certain degree of acceptable error levels.

During the last four decades there have been many developments in the interpretation of ERT techniques for data collected in two-dimensions [3], [4], [5] [6] and three-dimensions [7], [8]. The interpretation techniques mentioned above are mostly linear approximations of nonlinear ERT problems and highly dependent on the initial approximations [9]. Global optimization techniques such as simulated annealing and genetic algorithms do not need initial approximations [10]. However, for 2D and 3D interpretation, these approaches are not feasible. In sedimentary contexts, Akcr et al. [11] used hybrid genetic algorithms to build a structure-based resistivity inversion.Rücker[12] incorporated *a priori* information of structural constraints from seismic and borehole data to improve the quality of ERT images. After extracting the structural orientation from geological sections, Zhou et al. [13] used a model covariance matrix in order to improve the inversion findings. Robert G Aykroyd et al.[14] proposed a Bayesian approach to reconstruct the shape of a homogeneous resistivity based on monotonicity information.

The electrical inversion problem is complex because of its non-linear and ill-posed nature. The ability of deep neural networks (DNNs) to map nonlinear and complicated functions has been used to train on electromagnetic induction data to estimate the distribution of subsurface electrical conductivity [15]. This method used a fully convolutional network (FCN) to reconstruct the electromagnetic conductivity images. EMI inversion through the FCN enabled faster and more accurate estimation of lower-surface conductivity images. To determine the diffusion of resistivity, the right probabilistic link between the facies and the resistivity data is used to classify alluvial deposits. [16]. B. Liu et al. [17] addressed the problem of ambiguity in the apparent resistivity data because of its variant characteristic inherent behavior. They optimized the loss function to deal with false anomalies. This study achieved more accurate inversion results and improved the accuracy of the prediction for regions further from the surface layer. Similarly, a convolutional neural network with a three-layer SegNet architecture has been trained for apparent resistivity data and the models generated theoretically [18]. The encoder layer extracts the main low-resolution features. The decoders compensate for the loss of resolution resulting from the encoder layer. Regression is applied to give better results for mapping the resistivity inversion problem.

Based on efficient learning models, deep learning has outperformed iterative and non-iterative optimization techniques for ERT inverse problems and better image reconstruction with relatively fewer computations [19], [20]. Since back-propagation for Neural Networks (NN) belongs to the family of a stochastic algorithms, their training might not converge to global optima. To mitigate this, the Quantization of NNs enables computationally less expensive models, which are crucial for ubiquitous computing [21], [22], [23].

In our deep learning-based inversion of ERT presented here,

*Department of Earth Sciences, †Department of Electrical Engineering
Indian Institute of Technology Bombay, Maharashtra, India

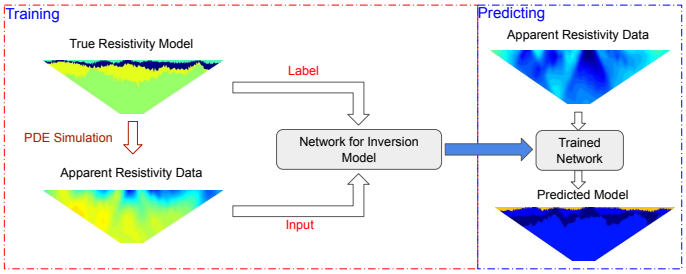

Fig. 1. Workflow of the deep learning resistivity models prediction algorithm. We have used the true resistivity model as label and apparent resistivity data as input to train our network. We aim to predict the resistivity model from apparent resistivity data using the trained network

CNNs are used directly in the inversion of ERT to learn the mapping between the input apparent resistivity data and the output true resistivity model. The present work implements the workflow in the two stages – training and prediction – as shown in Fig. 1. CNN-based Variational Auto Encoder (VAE) [24] is used as the foundation for our Variational Encoder-Decoder(VED) network, which incorporates residual blocks for a supervised task. We also compare our results with traditional UNet and Attention UNet architectures. After successfully developing the algorithm, we have applied it to the field data sets. We also compared our results with traditional inversion algorithms.

With our approach, we make the following contributions:

- To the best of our knowledge, we are the first to perform layered geological structures(as true resistivity model) for deep learning inversion studies.
- We show the importance of considering both apparent and true resistivity as different modalities for a deep learning model, rather than considering it as a segmentation task(where pixel-to-pixel mapping is required, which is not true in inversion due to the pseudo-depth).

This paper is organized into five main sections. Section I presents the introduction to ERT, background knowledge of the domain, and the scope of an inverse problem. Section II describes step-by-step implementation of the proposed methodology. Section III explains the experiments conducted and Section IV discusses the obtained results. Finally, the conclusions and future work are stated in Section V.

II. Methodology

In this section, we discuss the details of the traditional ERT models, ie. geophysical forward and inverse modeling formulations for the synthetic data generation and the detailed structure and training of the proposed deep neural network.

A. Forward modeling formulations

Ohm's law, which governs the flow of electric current in the ground, is the fundamental physical law used in resistivity studies. Ohm's law relates the current density J to the intensity of the electric field E and the electrical conductivity σ as shown in Equation 1:

$$J = \sigma E \tag{1}$$

Because of the conservatism of stationary electric fields, the relationship between electric potential and field intensity is given by

$$E = -\nabla\Phi \tag{2}$$

where Φ is the electric potential.

Combining equations 1 and 2, we get

$$J = -\sigma\nabla\Phi \tag{3}$$

All source-free regions must satisfy the continuity equation's requirement that J's divergence vanish.

$$\nabla \cdot J = 0 \tag{4}$$

For a point-like source of current, I at the position r_s its divergence $I\delta(\ r - \ r_s)$ has to be considered, leading to the governing equation 5

In the 2D DC resistivity forward modeling, the following elliptic equation is solved to calculate the potential distribution $\Phi(x, y, z)$ on a 2D conductivity structure σ due to a current source I

$$\nabla \cdot (\sigma\nabla\Phi) = -I(x, y, z) \tag{5}$$

We have used the finite element method to solve equation 5. Furthermore, we have calculated the apparent resistivity from the potential differences using the general approach of [25]. This results in a normalized potential difference that is equal to the system's response to unity. – Each electrode is assumed to be a current pole, and the potentials at each node are calculated accordingly. It is therefore possible to utilize any combination of current-potential electrodes to calculate the apparent resistivities. Pseudo-sections are used to display the apparent resistivity values.

Forward modeling plays a very important role in making inversion algorithms effective and stable. In discrete form, we represent it following using equation 6,

$$d^{pre} = F(m) \tag{6}$$

where, F is a forward modeling operator and $m = (\log\sigma_1, \log\sigma_1, ... \log\sigma_M)^T$ is a vector of model parameters, where σ_k is the conductivity of the k^{th} model parameter, M is the total number of triangles, and d^{pre} is the general type of data set, which is apparent resistivity in our case. Equation 6 relates the true resistivity/conductivity distribution with the apparent resistivity data sets. It can be used to perform traditional inversion as well as to train the deep learning model.

B. Constructing the Synthetic True Resistivity Model

A large number of data-model pairs are typically required to train a deep learning inversion network since it uses optimization of the network parameters to learn the nonlinear mapping. Training data and network design are critical to the success of deep learning approaches. According to Kawaguchi et al. [26] and Choromanska et al. [27], the convergence

point that deep learning methods could reach is closer to the global minimum under certain conditions. A fairly frequent understanding is that DL resistivity model inversion studies follow the "supervised learning paradigm," which calls for an enormous amount and variety of data with the desired labels. Data-driven techniques' performance is heavily dependent on the training data that are used. In order to train neural networks with nonlinear mapping capabilities, testing the model is critical for deep learning resistivity inversion. Good model design helps the trained neural network to be more likely to be deployable in realistic settings. Some studies [28], [29], [30] have collected their own data sets, including models with faults, salt bodies, and layered subsurface and trained their DL network on these models only i.e. faults, salt bodies and layered subsurface.

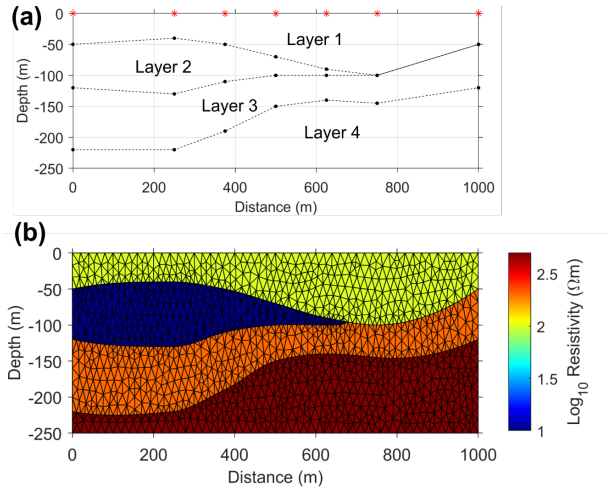

Fig. 2. (a)Control (red star) and construction (black) points to define the lithological interfaces and (b) corresponding constructed resistivity model generated using Delaunay triangulation.

To train the DL resistivity inversion, we constructed a resistivity model using a certain lithological unit, as shown in Fig. 2. Variable control points construct (shown by a red star and black dots) the resistivity model. Let $x_1, x_2, ..., x_n$ be the horizontal direction surface control points (red star). Now, at each control point, we assign the thickness of each geologic unit. If any geologic units are not present at some control points, the corresponding thickness values are assigned to zero. For example, we have assigned the thickness of the first lithologic unit as $layer1$=[50 40 50 70 90 100 50]; in a similar way, we have assigned the thickens of the second and third layer as $layer2$ = [70 60 50 30 10 0 0] and $layer3$ = [100 90 80 50 40 45 70], respectively. Here in the 2(a), values of control points are [0 250 375 500 625 750 1000]. Now, at this stage, we have assigned the true resistivity values in all four layers which are 100, 10, 200, and 500 ohm-m respectively. We have constructed a true subsurface resistivity model as shown in 2(b). The triangle quality is a measure of the acceptability of any triangle element and is expressed by Bank [31]

$$q = \frac{4A\sqrt{3}}{h_1^2 + h_2^2 + h_3^2} \tag{7}$$

Where h_1, h_2 and h_3 are sides and A is the area of a particular triangular cell. If $q > 0.6$, then the triangle is stated to be of acceptable quality[32]. The triangle quality is equal to one when all sides are equal. Detailed information on unstructured grids can be found in the study by [33], which describes a successful application to 2D magnetotelluric modeling.

C. Deep Learning Inversion

Convolutional neural networks are widely used deep learning models [34] which has the ability to extract the essential characteristics of patterns from the data and converge to a global optimum.

Let $x \epsilon R^{w \times h}$ denote the apparent resistivity data with the ground truth label $y \epsilon R^{w \times h}$. The image's width and height are denoted by w and h, respectively. The goal is to learn a robust inversion model $F(x, y : \theta)$ parameterized with that maps the resistivity from the input space x to the target space y. Deep CNNs are designed based on a large number of layers for the convolution process. The feature maps (Z) of the input data A can be obtained by:

$$Z = A * f + b \tag{8}$$

where $A \epsilon R(H, W, C)$ is the input data where H, W and C are height, width and the number of channels of A, respectively. In addition, f is the convolution filter for each layer, b is the bias parameter and * is the convolution operation. This procedure generates millions of parameters dependent on the size of the input data and the kernel of the filter, and these parameters can be adjusted in each layer.

Our proposed network is based on Variational Auto-Encoder [24]. A modified version of the Encoder-Decoder structure of the VAE is utilized for feature extraction. This system is a variational encoder-decoder (VED) network, since input and output are not identical, as would be in a standard VAE system[36]. The apparent data is fed into this network, and the network returns the true resistivity map as an output. PyTorch[37] is used to implement the network, and Fig. 3 presents a detailed structure of the network.

On the contracting path, the number of features doubles. Also downsampled by average-pooling, while in the expansive path the number of features is half. The encoder process decreases the feature map resolution to extract the best features of the original image, after that, the decoder module rebuilds the final map from these small feature maps to generate the final decision.

We considered residual blocks for both encoder and decoder. Each block of the VED model has structures including convolution, instance normalization, random leaky ReLU activation, and pooling layers as encoder path and a decoder path with upsample layers.

The encoding model is denoted as $q_\phi(z|x)$, where z is the latent embedding paired with spatial information and $x = f_\gamma(i)$ is semantics from the input image i's high-level feature. $p_\theta(m|z)$ is a probabilistic decoder that outputs the 2-D grid true resistivity mapping m from the latent embedding

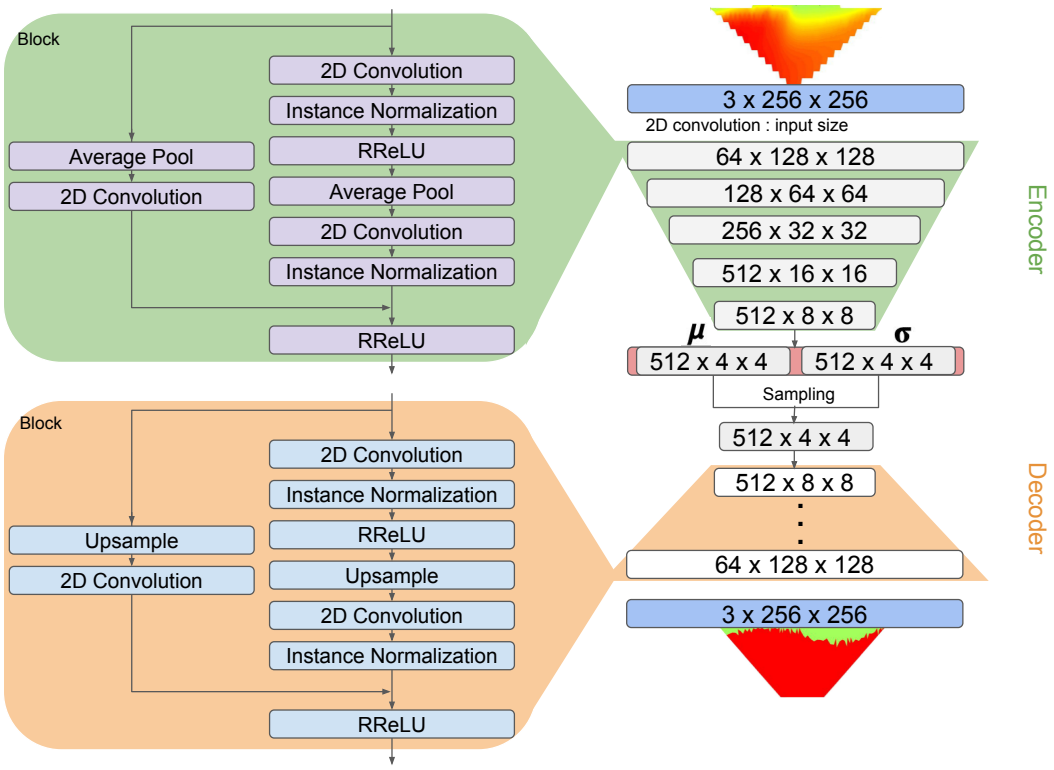

Fig. 3. Model architecture of encoder in variational encoder-decoder (VED) consists of five layers of convolutional neural network (CNN). Each encoder and decoder layer is a residual block [35]. At the end of the encoder, the extracted data are converted into mean and standard deviation values with a size of 512 x 4 x 4. The latent variable is sampled from the values of mean and standard deviation. The hyperparameter of the decoder is set symmetrically so that the output size is the same as that of the encoder.

z. It is possible to learn the parameters (γ,ϕ,θ) of the neural networks f, q, or p simultaneously using end-to-end training.

The latent loss increases when the latent embedding z is forced to follow the usual normal distribution. The Kullback-Leibler divergence between z and $N(0, I)$ is referred to as L_{latent}. Reconstruction loss is defined as the Mean Squared Error (MSE) between the mapped prediction output layer and the ground truth.

We also considered perceptual loss $L_{perceptual}$. The idea behind perceptual loss in image similarity is that if people think one image looks more like the original, it should also result in a lesser loss [38]. Deep features from a pre-trained VGG-19 are used as a stand-in for the perception of the prediction mapping and ground truth of an image.

So the overall loss L for training is the combination of latent loss, reconstruction loss, and perceptual loss:

$$L = L_{Reconstruction} + L_{latent} + L_{perceptual} \tag{9}$$

We train all considered networks using Adam optimizer with learning rate = 0.0001, and mini-batch sizes of 20 for 100 epochs.

D. Deterministic Inversion of ERT data

To compare the results of deep learning inversion, we have also developed a traditional inversion framework to interpret the datasets. We have used the same forward formulation as describe in the section A. Since direct current resistivity inverse problems are a highly underdetermined problem. We introduced an additional term named model regularization term $\phi_m(m)$ along with data misfit function $\phi_d(m)$ using Tikhonov parametric function [39]. Further, these two terms will be weighted by a regularization term λ_1 and yield the minimization function

$$\min_m(\phi^{total}) = \phi^d + \lambda_1\phi^m, \epsilon\phi^d <= \phi^\epsilon \tag{10}$$

where ϕ^ϵ is the target misfit. The regularization term λ_1 is a very important term and controls the tradeoff between model regularization and data misfit function. Experience or the "trial-and-error" method will yield an accurate regularization parameter value. A greater regularization parameter was evaluated with a damping factor of 0.5, which decreased to a minimum of 0.01 in subsequent iterations.

The data misfit function is the quantitative measurement of the difference between the observed apparent resistivity data d^{obs} and the predicted data d^{pre}. Predicted data is the mathematical model F(m), where F is derived through numerical modeling using equations 5 and 6. The mathematical representation of the data misfit function is

$$\phi^d = ||W^d(F(m) - d^{obs})||_2^2 \tag{11}$$

where $||.||_2^2$ is the l^2 norm. $W^d = diag1/\sigma_1^2, 1/\sigma_2^2, ...1/\sigma_M^2$ and $_i$ is the individual standard deviation of the i^{th} observation.

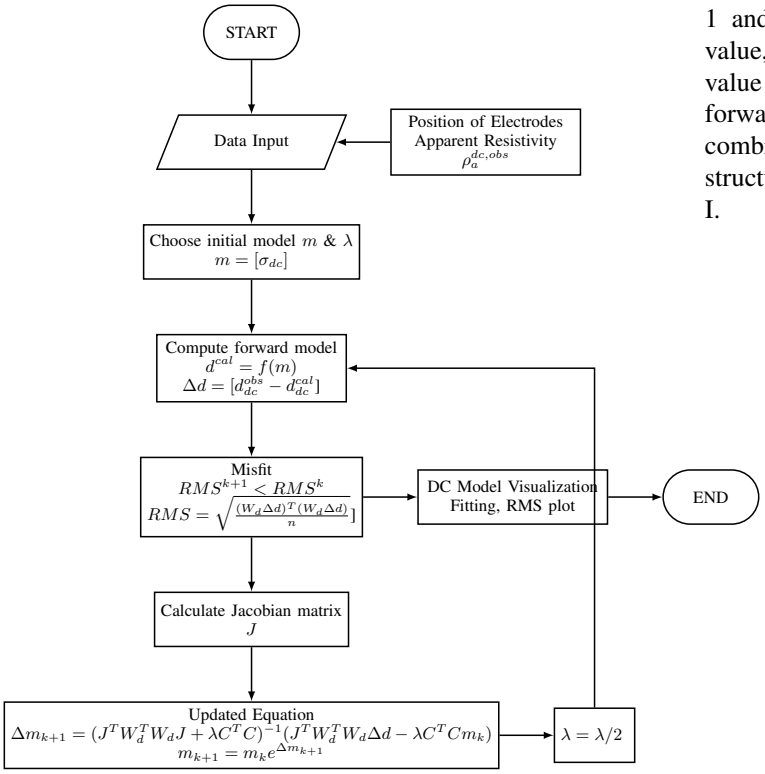

Fig. 4. Inversion flow-chart of the deterministic approach. In the present work, we have modified the inversion code of Singh et al.[40] to the triangular grids.

To control the difficulty of the recovered resistivity model, we have formulated our regularization term according to Li and Oldenburg [9]

$$\phi^m = ||\alpha_1 W_s^m (m - m^{ref})||_2^2 + ||W^m m||_2^2 \qquad (12)$$

Where the m^{ref} is the reference model (i.e. a priori known resistivity model) and the matrix W_s^m is the diagonal matrix containing block weights. Weighting matrices $W_i^m (i = 2, 3, 4)$ are the finite-difference x-direction gradient component, z-direction gradient component, and Laplace's differential component.Figure 4 is the flowchart of the ERT inversion which we have developed for the deep learning model.

III. Experiments

A. Dataset

We generated 24,000 apparent and true resistivity image pairs for the experiment. We created various models by changing the locations of the control points, the thickness of each resistivity layer at the control points, and resistivity values at each layer as shown in Fig. 2. We consider different layer structures such as uniform resistivity values, where all 4 layers have a single resistivity value. In 2 layers it will have 2 different random resistivity values, where the layer combinations are considered as shown in the TABLE II. Whichever layers are within brackets (.), we consider them together with same resistivity value. In two-layer combinations, we considered either the first layer with a resistivity value and a combination of (2,3,4) with another resistivity value, 1 and 2 layers combined together with a single resistivity value, and 3 and 4 layers combined with a single resistivity value create another two-layer combination, etc. Through forward modeling as explained in section II-B In each layer combination, we generated 2000 image pairs. For each layer structure, the total generated data pairs are shown in TABLE I.

TABLE I
DATA GENERATED

Layers	No of data pairs
Uniform	2000
2 layer	6000
3 layer	6000
4 layer	10000

TABLE II
LAYER COMBINATIONS

Layer	Combinations
Uniform	[(1,2,3,4)]
2 Layer	[1,(2,3,4)], [(1,2),(3,4)], [(1,2,3),4]
3 Layer	[1,2,(3,4)], [1,(2,3),4], [(1,2),3,4]
4 Layer	[1,2,3,4]

Dataset was also divided into 80:10:10 for training, validation, and testing.

B. Baseline Methods

To compare the results of our VED model, we considered the vanilla UNet and Attention UNet architectures. We also considered a depth-map layer to the input apparent data as mentioned by B.Liu et al. [17]. A depth map to encode the position information for the apparent resistivity created in such a way that, each pixel row will have a fixed value, which increases from top to bottom of the image as shown in Fig 5. We create the depth map by setting the values for each layer as $value = 1$ for the top row, and $value = 2$ for the next row, and similarly, we continued increasing values with increasing depth.

Fig. 5. Depth input map is with a structure that element in each rows has the value equal to a number, and which increases while going down the row

1) UNet: We design our networks based on a widely used U-Net encoder-decoder neural architecture. U-Net gets its name due to its contracting path followed by an expansive path. At each max pooling step in the contracting path, downsampling occurs which doubles the number of features, while the number of features is halved in the expansive path by upsampling. Across the downsampling and upsampling layers, a copy and crop of the features are performed that combines low-level feature maps (from the shallow layers) to the high-level feature maps (from the deep layers) through skip connections to bring the spatial context in the lower-level (finer) details. This allows retention of high-frequency detail for sharp class boundaries. The detailed architecture of the UNet considered is shown in Fig. 6

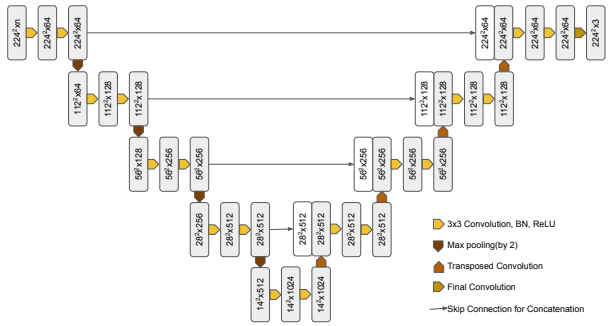

Fig. 6. UNet Architecture Applied. 'n' is the number of input bands n = 4 when with the depth band, n = 3 without the depth bands.

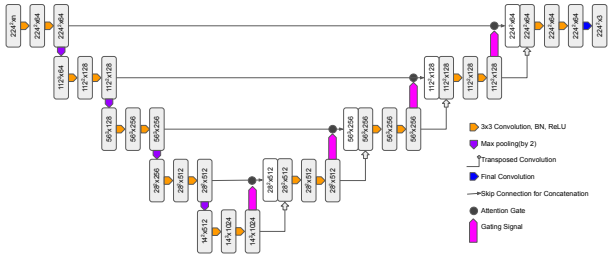

Fig. 7. Attention UNet architecture [41]. 'n' is the number of input bands n = 4 when with a depth band, n = 3 without depth bands. The numbers within each block represent the feature maps with (spatial dimension)^2 x the number of channels. Orange arrow represents convolutional layer. Purple arrow means max-pooling operation which downsamples feature maps, while transparent arrow means transposed convolution which upsamples feature maps. Black arrow is the shortcut which concatenates feature maps from shallow layers to deep layers.

2) Attention UNet: Attention, in the context of computer vision, is a way to highlight only the relevant activations during training, which reduces the computational requirements by avoiding irrelevant activations. [41] That is, certain parts of the images will get more "attention" from the network based on attention gates as areas of high relevance that are multiplied with a larger weight, while the areas of low relevance are multiplied with smaller weights. As the model is trained, more focus is given to the regions with higher weights. The detailed architecture of Attention UNet considered is shown in Fig. 7

C. Evaluation metric

The metrics we used were the coefficient of determination, Pearson correlation coefficient, and cosine similarity for evaluating our method. For these metrics, larger values imply better performance.

Coefficient of Determination (R^2): R^2 is the proportion of the variation in the dependent variable that is predictable from the independent variables, given by

$$R^2(y,\hat{y}) = 1 - \frac{\sum_{i=1}^{n}(y_i-\hat{y}_i)^2}{\sum_{i=1}^{n}(y_i-\bar{y})^2}, \tag{13}$$

where $\bar{y} = \frac{1}{n}\sum_{i=1}^{n} y_i$ and $\sum_{i=1}^{n}(y_i-\hat{y}_i)^2 = \sum_{i=1}^{n}\epsilon_i^2$.

Pearson Correlation Coefficient (PCC): PCC is a measure of linear correlation between two sets of data, given by

$$PCC = \frac{Cov(y,\hat{y})}{\sigma_y \sigma_{\hat{y}}} \tag{14}$$

where Cov is the covariance and σ is the standard deviation.

Cosine Similarity (CS): CS is a measure of similarity between two non-zero vectors of an inner product space given by

$$CS(y,\hat{y}) = \frac{y.\hat{y}}{\|y\|.\|\hat{y}\|}, \tag{15}$$

where y is the ground truth and $\hat{y}$ is the model prediction.

D. Error metrics

There are error metrics like mean squared log error, root mean squared error, and mean absolute error that can be used to evaluate the performance of these methods. For error-based metrics, smaller values imply better performance.

Mean Squared Log Error (MSLE): MSLE computes a risk metric corresponding to the expected value of the squared logarithmic (quadratic) error, given by

$$\text{MSLE}(y,\hat{y}) = \frac{1}{n_{\text{samples}}}\sum_{i=0}^{n_{\text{samples}}-1}(\log_e(1+y_i) - \log_e(1+\hat{y}_i))^2. \tag{16}$$

Mean Squared Error (MSE): MSE represents the second sample moment of the differences between predicted values and observed values. , given by

$$\text{RMSE}(y,\hat{y}) = \frac{1}{n_{\text{samples}}}\sum_{i=0}^{n_{\text{samples}}-1}(y_i-\hat{y}_i)^2. \tag{17}$$

Mean Absolute Error (MAE): MAE is the arithmetic average of the absolute errors, given by

$$\text{MAE}(y,\hat{y}) = \frac{1}{n_{\text{samples}}}\sum_{i=0}^{n_{\text{samples}}-1}|y_i-\hat{y}_i|. \tag{18}$$

IV. Results

A. Synthetic Datasets

The evaluation metrics on test dataset is shown in TABLE III and error metrices of the same on the TABLE IV. In it, 'UNet D' represents the UNet with depth layer input. 'A UNet' represents the attention UNet, and 'A UNet D' represents the attention UNet with depth layer. For both evaluation metrices

and error metrices, our method(VED) for inversion performs far better than the compared onces.

A set of samples from the test data set is taken and tested on the mentioned networks and the corresponding results are shown in Fig. 8. Here, the rows from top to bottom represent the uniform resistivity model, 2 layer, 3 layer and 4 layer resistivity models, respectively. For each layer considered, the inverted results from the VED outperform other network predictions.

Table V shows the comparison of the number of training parameters for each deep learning architecture considered. Compared to UNet and attention UNet, which have 31 million trainable parameters, our approach with variational encoder-decoder architecture gives better results with 22 million trainable parameters.

TABLE III
EVALUATION METRICS: UNET, ATTENTION-UNET RESULTS FOR WITH AND WITHOUT DEPTH LAYERS, AND VED

	UNet	UNet D	A UNet	A UNet D	VED(Our)
R^2	0.8882	0.8529	0.8848	0.8926	**0.9519**
PCC	0.9350	0.9481	0.9399	0.9351	**0.9938**
CS	0.9785	0.9780	0.9804	0.9782	**0.9974**

TABLE IV
ERROR METRICES: UNET, ATTENTION-UNET RESULTS FOR WITH AND WITHOUT DEPTH LAYERS, AND VED

	UNet	UNet De	A UNet	A UNet D	VED(Our)
MSLE	0.0083	0.0116	0.0083	0.0083	**0.0007**
MSE	0.0219	0.0170	0.0161	0.0173	**0.0033**
MAE	0.0643	0.0723	0.0606	0.0521	**0.0174**

B. Geology of the region and data collection

The study area belongs to the West Medinipur district of West Bengal, India, as shown in Fig. 9. The latitude and longitude of the northern and southern points are 21 ° 45 N 86 ° 45 E and 23 ° 00 N 88 ° 00 45 E, respectively. Three types of geological formations belong from the Proterozoic to the Quaternary age. They are lateritic terrains, consolidated crystalline rocks, and unconsolidated to semi-unconsolidated tertiary sand and gravel. The western part of the Medinipur district has crystalline rocks marked red in figure 9. The groundwater mainly exists in the weathered residuum within 10 m of the surface and in fractures within 65 m of the surface in such formations. Unconsolidated/older alluvium is the source of West-laterite Medinipur's landscapes. Laterites top the aquifer in earlier alluvium, which has a maximum thickness of 50 meters. The tertiary sand and gravel-type formation is found at a depth of 100 to 140 m below this older alluvium. It has a lot of groundwater due to its porous nature. Hard rock underneath water levels drop during dry seasons. The flat alluvial and deltaic plains are present in the east and southeast of the district [42] [43] The deltaic planes are formed by younger alluvium. Groundwater levels in these formations are much higher than those in previous alluvial deposits. The Kangsabati and Subarnarekha rivers form the backbone of the research area. (Fig. 9).

TABLE V
COMPARISON OF NETWORKS ON TRAINABLE PARAMETERS

Network	No.of trainable parameters (in Millions)
UNet	31.04
Attention UNet	31.39
VED(our)	22.89

Generally speaking, the research area has two distinct hydro-geological areas. The older alluvium is on top of the secondary laterite-covered fluvial-deltaic deposits. The aquifer beneath the flood plain is primarily composed of sands and silts, with only a trace proportion of clays. In April and May, the hottest temperatures are reported, and the coldest are recorded in February and January. The principal sources of groundwater recharge in the study area are rainwater and river water. Multi-electrode electrical resistivity surveys using Wenner configuration were performed using 10 m electrode spacing (Fig. 10(a)). The total length of the profile is 800 m and is marked as "ERT Profile" in Fig. 9. The resistance values of each electrode are shown in Fig. 10(b). Apparent resistivity pseudo section of the field data is shown in Fig. 10(c). Minimum and maximum apparent resistivity values were 22 and 190 ohm-m, respectively.

C. Comparison of Inverted Resistivity model with DL

To test the efficacy of deep learning, we have first inverted the field data using the deterministic inversion approaches which flowchart has been shown in the Fig. 4. Fig. 12(a) is the inverted resistivity modes using deterministic minimization approaches [40] We interpreted the four different geologic units from the inverted 2D resistivity model namely (1) soil (50–100 m), (2) compact laterite, (10–100 m), soft laterite (10–100 m), and coarse sand and gravel (10-20). The high resistivity zone between 450-800 m along the profile and 10-50 m depth is soft and compact laterite, which is shown with the blue color in Figure 12(a). Here, we would like to highlight that compact laterite is very problematic in terms of groundwater recharge.

The computed apparent resistivity pseudo-section is shown in Figure 11(a). It is clear that the computed apparent resistivity pseudo-section (Figure 11(a)) is nearly identical to the observed apparent resistivity pseudo-section (Figure 10(c)).

We performed five experiments, using our VED approach, two for UNet and two for Attention-UNet architecture, using the synthetic apparent resistivity image data. Our proposed approach accomplished significantly improved outcomes for mapping the subsurface's true resistivity from the apparent resistivity compared to traditional inversion. A comparison of results for field data is shown in Fig. 12.

One of the significant issues with the resistivity model obtained via traditional inversion is that it is highly dependent on the initial guess and choices of the norm.

We noted that our inverted resistivity models of our DL method (VED) accurately produced the topsoil layer (approx-

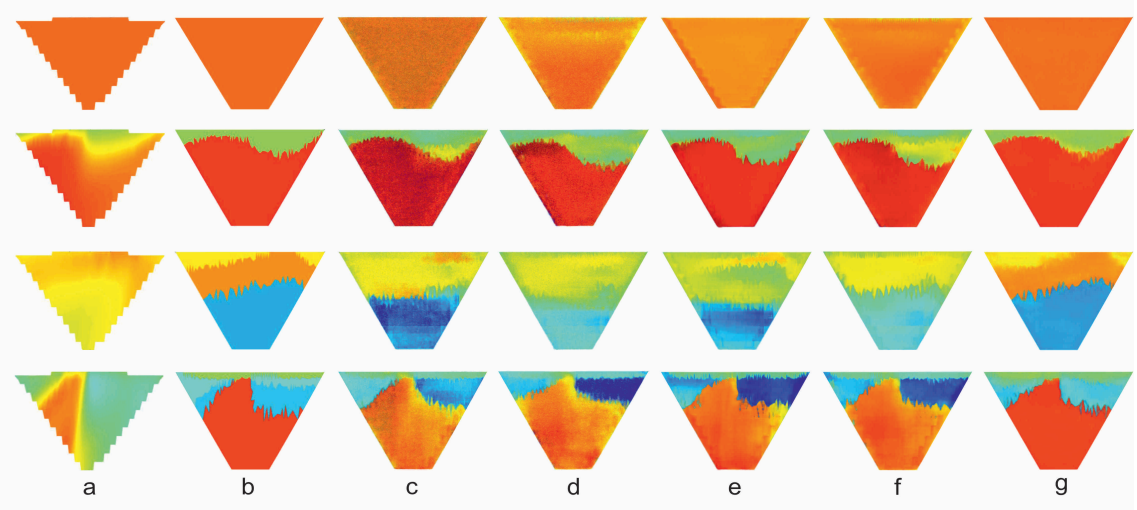

Fig. 8. Synthetic test sample results: The first column(a) is the apparent input data to the network. Second column(b) is the ground truth true resistivity. The third(c), fourth(d), fifth(e), sixth(f) and seventh(g) columns are the interpreted models from UNet, UNet with depth layer, Attention UNet, Attention UNet with depth layer and VED(our) respectively. Each row represents Uniform, 2 layer, 3 layer, 4 layer respectively from top to bottom

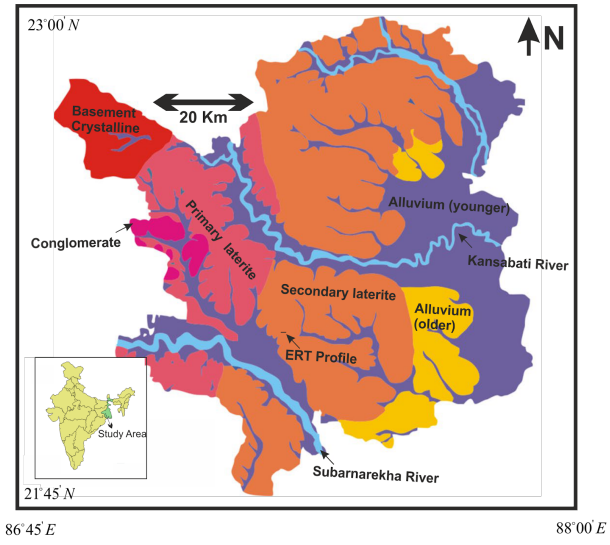

Fig. 9. The geology of the study area belongs to the West Medinipur district of West Bengal, India.

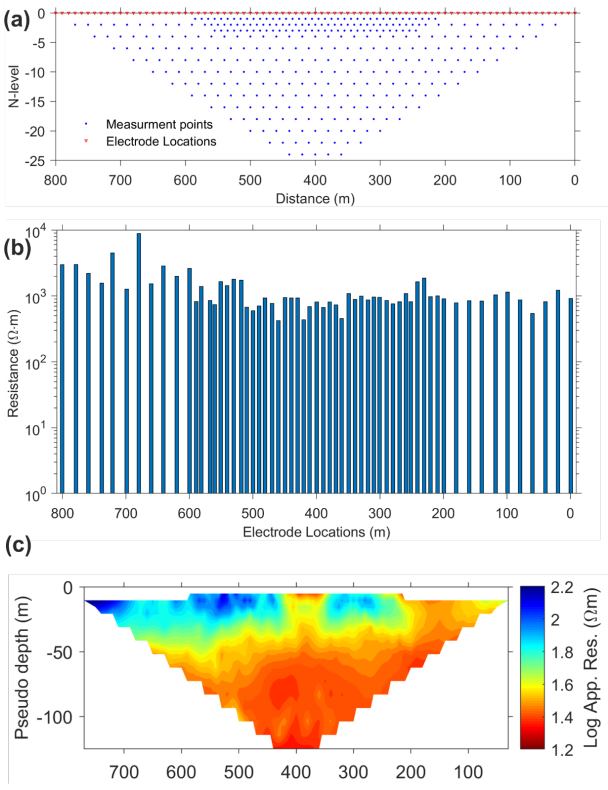

Fig. 10. (a) Electrode locations and their corresponding collected data using the Wenner configuration. (b) The resistance value of each current electrode. (c) Contour plot of the collected apparent resistivity data shown in Fig. 8a.

imately 7 m, see Fig. 13), which was not evident in traditional inversion (Fig. 12 (a)). It happens because apparent resistivity data are insensitive to the top 10m as the minimum current electrode separation is 30m. Thus, our proposed approach achieved significantly improved results in mapping the true resistivity of the subsurface from the apparent resistivity compared to traditional inversion. However, we have noted that among all deep learning architectures, our variational encoder-decoder produces more geological relevant models with higher R2 values. Fig. 13 shows the comparison of inverted and deep learning resistivity models at 610 m locations of ERT profile. The first and second columns are the lithology obtained from the tubewell and the traditional inversion. The rest of the columns are the lithology obtained from DL. In Fig. 13, our VED network inversion has predicated the topsoil layer. However, traditional inversion fails to do this and assigns it as a compact laterite. The resistivity of the soft laterite (10–100 ohm m) and coarse sand and gravel (10-20 ohm-m) are very close to each other; DL also faces difficulty differentiating these two geologic units, also UNet and attention UNet architectures fail to predict the coarse sand and gravel at the bottom, but the VED was able to predict that too.

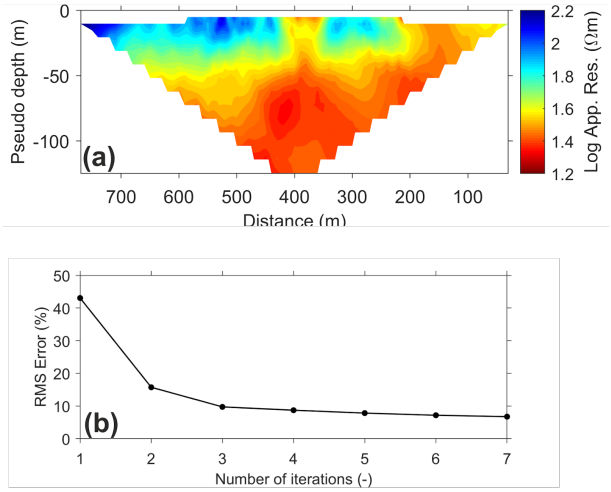

Fig. 11. (a) Modeled apparent resistivity pseudo-section corresponding to the resistivity models shown in Fig. 9. (b) Convergence pattern of the inversion. We stopped the inversion when the root mean square error was no longer reduced.

V. Conclusions

This paper describes a novel method to obtain an actual resistivity distribution from two-dimensional apparent resistivity data sets. First, we develop a Gauss-Newton minimization approach on the unstructured grid. The synthetic example noted that the inverted resistivity models are either lower or higher than the actual resistivity models due to an inversion algorithm. Also, the inverted images were blurry. Consequently, we can identify the geologic units on the relative scale on the basis of the inverted resistivity models. We have developed a novel deep learning algorithm to interpret the ERT datasets to overcome this.

In the present work, we have trained our network architecture using the variational encoder-decoder consisting of five layers of a convolutional neural network. We have trained our network with 24,000 pairs of apparent resistivity datasets and true resistivity models. For that we have developed an automated algorithm that can generate various models by changing the locations of the control points and the thickness and resistivity of each layer at the control points.

The synthetic example shows that our VED network architecture provides better inverted resistivity models than the UNet, UNet with depth layer, Attention UNet, and Attention UNet with depth layer models. Also, our results very close to the ground truth, as determined using actual data . These results are consistent for the homogeneous, two-layer, three-layer, and four-layer resistivity models. In the field data case, our results were also very consistent and the network achieved with an R^2 score of 0.95. . These results are consistent for the homogeneous, two-layer, three-layer, and four-layer resistivity models.

Acknowledgment

BW would like to thank the Ministry of Education, Government of India, for financial assistance in the form of a Research Fellowship. This work is part of doctoral dissertation of BW. AS is extremely grateful to IRCC-IITB for the financial support to carry out this study in the form of a seed grant project (project code RD/0518-IRCCSH0-022).

References

[1] A. Perrone, V. Lapenna, and S. Piscitelli, "Electrical resistivity tomography technique for landslide investigation: A review," *Earth-Science Reviews*, vol. 135, pp. 65–82, 2014.

[2] A. Tarantola, *Inverse problem theory and methods for model parameter estimation*. SIAM, 2005.

[3] S. Boonchaisuk, C. Vachiratienchai, and W. Siripunvaraporn, "Two-dimensional direct current (dc) resistivity inversion: Data space occam's approach," *Physics of the Earth and Planetary Interiors*, vol. 168, no. 3-4, pp. 204–211, 2008.

[4] C. Rücker and T. Günther, "The simulation of finite ert electrodes using the complete electrode model," *Geophysics*, vol. 76, no. 4, pp. F227–F238, 2011.

[5] M. Loke and R. Barker, "Practical techniques for 3d resistivity surveys and data inversion1," *Geophysical prospecting*, vol. 44, no. 3, pp. 499–523, 1996.

[6] I. Akca, "Elris2d: A matlab package for the 2d inversion of dc resistivity/ip data," *Acta Geophysica*, vol. 64, no. 2, pp. 443–462, 2016.

[7] T. Günther and C. Rücker, "A general approach for introducing information into inversion and examples from dc resistivity inversion," in *Near Surface 2006-12th EAGE European Meeting of Environmental and Engineering Geophysics*. European Association of Geoscientists & Engineers, 2006, pp. cp–14.

[8] A. Pidlisecky, E. Haber, and R. Knight, "Resinvm3d: A 3d resistivity inversion package," *Geophysics*, vol. 72, no. 2, pp. H1–H10, 2007.

[9] Y. Li and D. W. Oldenburg, "3-d inversion of gravity data," *Geophysics*, vol. 63, no. 1, pp. 109–119, 1998.

[10] S. P. Sharma, "Vfsares—a very fast simulated annealing fortran program for interpretation of 1-d dc resistivity sounding data from various electrode arrays," *Computers & Geosciences*, vol. 42, pp. 177–188, 2012.

[11] I. Akça and A. T. Basokur, "Extraction of structure-based geoelectric models by hybrid genetic algorithms," *Geophysics*, vol. 75, no. 1, pp. F15–F22, 2010.

[12] C. Rücker, "Advanced electrical resistivity modelling and inversion using unstructured discretization," Ph.D. dissertation, Universität Leipzig, 2010.

[13] J. Zhou, A. Revil, M. Karaoulis, D. Hale, J. Doetsch, and S. Cuttler, "Image-guided inversion of electrical resistivity data," *Geophysical Journal International*, vol. 197, no. 1, pp. 292–309, 2014.

[14] R. G. Aykroyd, M. Soleimani, and W. R. Lionheart, "Conditional bayes reconstruction for ert data using resistance monotonicity information," *Measurement Science and Technology*, vol. 17, no. 9, p. 2405, 2006.

[15] D. Moghadas, "One-dimensional deep learning inversion of electromagnetic induction data using convolutional neural network," *Geophysical Journal International*, vol. 222, no. 1, pp. 247–259, 2020.

[16] T. Hermans and J. Irving, "Facies discrimination with electrical resistivity tomography using a probabilistic methodology: effect of sensitivity and regularisation," *Near Surface Geophysics*, vol. 15, no. 1, pp. 13–25, 2017.

[17] B. Liu, Q. Guo, S. Li, B. Liu, Y. Ren, Y. Pang, X. Guo, L. Liu, and P. Jiang, "Deep learning inversion of electrical resistivity data," *IEEE Transactions on Geoscience and Remote Sensing*, vol. 58, no. 8, pp. 5715–5728, 2020.

[18] M. Vu and A. Jardani, "Convolutional neural networks with segnet architecture applied to three-dimensional tomography of subsurface electrical resistivity: Cnn-3d-ert," *Geophysical Journal International*, vol. 225, no. 2, pp. 1319–1331, 2021.

[19] A. Krizhevsky, I. Sutskever, and G. E. Hinton, "Imagenet classification with deep convolutional neural networks," *Advances in neural information processing systems*, vol. 25, 2012.

[20] G. Wang, J. C. Ye, K. Mueller, and J. A. Fessler, "Image reconstruction is a new frontier of machine learning," *IEEE transactions on medical imaging*, vol. 37, no. 6, pp. 1289–1296, 2018.

[21] Y. Li, X. Dong, and W. Wang, "Additive powers-of-two quantization: An efficient non-uniform discretization for neural networks," *arXiv preprint arXiv:1909.13144*, 2019.

[22] D. Miyashita, E. H. Lee, and B. Murmann, "Convolutional neural networks using logarithmic data representation," *arXiv preprint arXiv:1603.01025*, 2016.

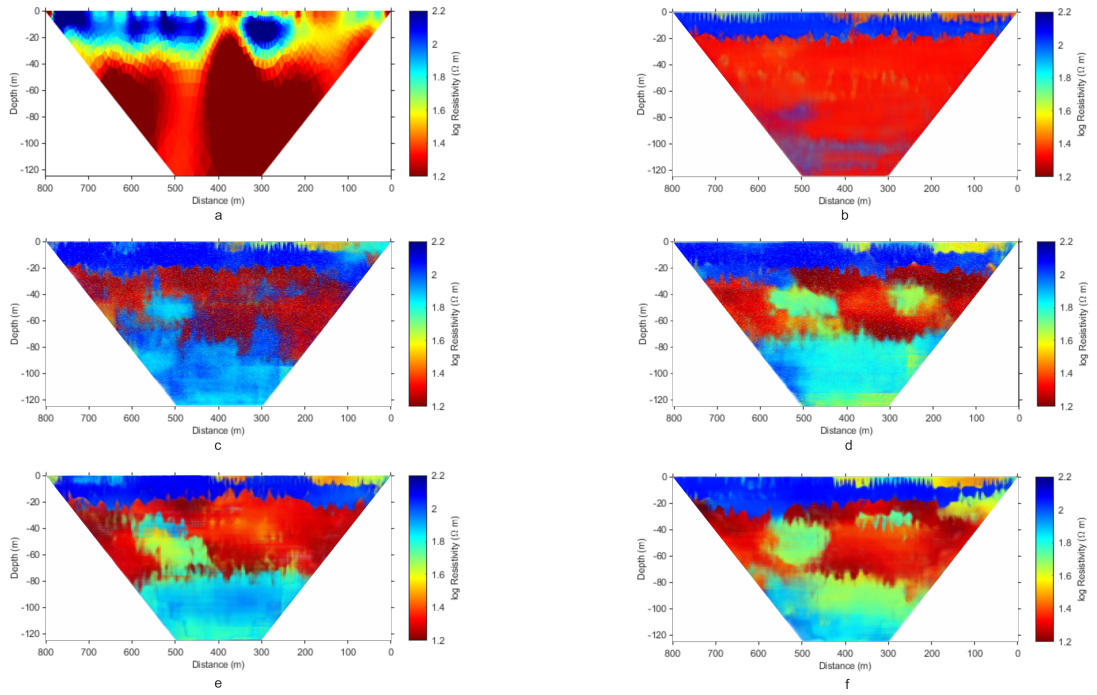

Fig. 12. The result of the inverted tomography over the field data shown in Fig.10c. The resistivity models obtained using is (a) Traditional Inversion, (b) VED(Our), (c) UNet, (d) UNet with depth, (e) Attention UNet and (f) Attention UNet with depth .

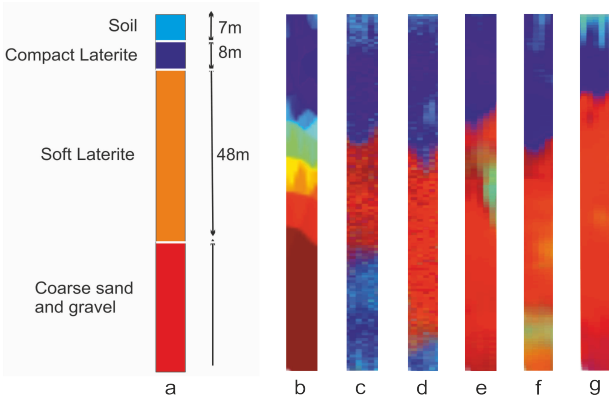

Fig. 13. Comparison of inverted and deep learning resistivity models at 610 m locations of the ERT profile. The first columnar is the lithology obtained from the tubewell. The second(b), third(c), fourth(d), fifth(e), sixth(f), and seventh(g) columnars are the interpreted models from traditional inversion, UNet, UNet with depth layer, Attention UNet, Attention UNet with depth layer, and VED(our) respectively.

[23] J. Choi, Z. Wang, S. Venkataramani, P. I.-J. Chuang, V. Srinivasan, and K. Gopalakrishnan, "Pact: Parameterized clipping activation for quantized neural networks," *arXiv preprint arXiv:1805.06085*, 2018.

[24] D. P. Kingma and M. Welling, "Auto-encoding variational bayes," *arXiv preprint arXiv:1312.6114*, 2013.

[25] L. Marescot, S. Rigobert, S. P. Lopes, R. Lagabrielle, and D. Chapellier, "A general approach for dc apparent resistivity evaluation on arbitrarily shaped 3d structures," *Journal of Applied Geophysics*, vol. 60, no. 1, pp. 55–67, 2006.

[26] K. Kawaguchi, "Deep learning without poor local minima," *Advances in neural information processing systems*, vol. 29, 2016.

[27] A. Choromanska, M. Henaff, M. Mathieu, G. B. Arous, and Y. LeCun, "The loss surfaces of multilayer networks," in *Artificial intelligence and statistics*. PMLR, 2015, pp. 192–204.

[28] Y. Wu and Y. Lin, "Inversionnet: A real-time and accurate full waveform inversion with cnns and continuous crfs," *arXiv preprint arXiv:1811.07875*, 2018.

[29] F. Yang and J. Ma, "Deep-learning inversion: A next-generation seismic velocity model building method," *Geophysics*, vol. 84, no. 4, pp. R583–R599, 2019.

[30] S. Li, B. Liu, Y. Ren, Y. Chen, S. Yang, Y. Wang, and P. Jiang, "Deep-learning inversion of seismic data," *arXiv preprint arXiv:1901.07733*, 2019.

[31] R. E. Bank, *Pltmg: A software package for solving elliptic partial differential Equations: Users' Guide 8.0*. SIAM, 1998.

[32] ——, "Pltmg: A software package for solving elliptic partial differential equations. users' guide 9.0," 2004.

[33] K. Key and C. Weiss, "Adaptive finite-element modeling using unstructured grids: The 2d magnetotelluric example," *Geophysics*, vol. 71, no. 6, pp. G291–G299, 2006.

[34] N. Aloysius and M. Geetha, "A review on deep convolutional neural networks," in *2017 international conference on communication and signal processing (ICCSP)*. IEEE, 2017, pp. 0588–0592.

[35] K. He, X. Zhang, S. Ren, and J. Sun, "Deep residual learning for image recognition," in *Proceedings of the IEEE conference on computer vision and pattern recognition*, 2016, pp. 770–778.

[36] C. Lu, M. J. G. van de Molengraft, and G. Dubbelman, "Monocular semantic occupancy grid mapping with convolutional variational encoder–decoder networks," *IEEE Robotics and Automation Letters*, vol. 4, no. 2, pp. 445–452, 2019.

[37] A. Paszke, S. Gross, F. Massa, A. Lerer, J. Bradbury, G. Chanan, T. Killeen, Z. Lin, N. Gimelshein, L. Antiga, A. Desmaison, A. Kopf, E. Yang, Z. DeVito, M. Raison, A. Tejani, S. Chilamkurthy, B. Steiner, L. Fang, J. Bai, and S. Chintala, "Pytorch: An imperative style, high-performance deep learning library," in *Advances in Neural Information Processing Systems 32*, H. Wallach, H. Larochelle, A. Beygelzimer, F. d'Alché-Buc, E. Fox, and R. Garnett, Eds. Curran Associates, Inc., 2019, pp. 8024–8035. [Online]. Available: http://papers.neurips.cc/paper/9015-pytorch-an-imperative-style-high-performance-deep-learning-library.pdf

[38] J. Johnson, A. Alahi, and L. Fei-Fei, "Perceptual losses for real-time style transfer and super-resolution," in *European conference on computer vision*. Springer, 2016, pp. 694–711.

[39] A. N. Tikhonov, V. I. Arsenin, V. Arsenin *et al.*, *Solutions of ill-posed problems*. Vh Winston, 1977.

[40] A. Singh, S. P. Sharma, İ. Akca, and V. C. Baranwal, "Fuzzy constrained

lp-norm inversion of direct current resistivity data," *Geophysics*, vol. 83, no. 1, pp. E11–E24, 2018.

[41] O. Oktay, J. Schlemper, L. L. Folgoc, M. Lee, M. Heinrich, K. Misawa, K. Mori, S. McDonagh, N. Y. Hammerla, B. Kainz *et al.*, "Attention u-net: Learning where to look for the pancreas," *arXiv preprint arXiv:1804.03999*, 2018.

[42] G. Pati, "Ground water year book of west bengal and andaman and nicobar islands," Technical report: Series 'D', Central Ground Water Board Ministry of Water ..., Tech. Rep., 2013.

[43] G. S. Bhunia, S. Samanta, D. K. Pal, and B. Pal, "Assessment of groundwater potential zone in paschim medinipur district, west bengal–a meso-scale study using gis and remote sensing approach," *Assessment*, vol. 2, no. 5, pp. 41–59, 2012.